Traveling carrier-density waves in *n*-type GaAs at low-temperature impurity breakdown

M. Gaa and E. Schöll
Institut für Theoretische Physik, Technische Universität Berlin, Hardenbergstraße 36, D-10623 Berlin, Germany
(Received 15 July 1996; revised manuscript received 13 September 1996)

We present a model for traveling charge-density wave instabilities in a semiconductor revealing *S*-shaped negative differential conductivity. It is based on microscopic generation-recombination rates including impurity impact ionization, which are obtained from Monte Carlo simulations. By a linear stability analysis and by numerical solution of the full nonlinear system we show that traveling-wave instabilities occur in the regime of both negative and positive differential conductivity. Our simulations give detailed insight into the spatiotemporal dynamics of the instabilities, and explain self-generated small-amplitude oscillations observed at the onset of breakdown. [S0163-1829(96)07448-6]

I. INTRODUCTION

Traveling-wave instabilities are common in a variety of nonlinear distributed active media far from equilibrium ranging from hydrodynamic and optical to chemical reaction systems and solids.[1,2] Recently, much attention has been paid to nonlinear spatiotemporal dynamics in semiconductor transport[3–5] where a menagerie of bifurcation scenarios have been observed.[6–10] The current density j versus electric field $\mathcal{E}$ characteristics often exhibit negative differential conductivity (NDC) classified as NNDC or SNDC, if the $j(\mathcal{E})$ relation is *N* shaped or *S* shaped, respectively. NNDC and SNDC are commonly associated with longitudinal and transverse spatial instabilities,[11] respectively, leading to electric field domains[12–18] or current filaments,[19–26] as was shown theoretically for different semiconductor models.

In this paper we demonstrate that this division need not always hold; more specifically, that a longitudinal traveling wave instability may also occur in the SNDC case, and that not even NDC is required. Our model system is *n*-type GaAs in the regime of impurity impact ionization breakdown. Based on the linear stability of the steady states, it has been argued for quite a while that current instabilities at finite wavelengths and frequencies should occur both in regimes of negative *and* positive differential conductivity.[19,27]

A first detailed linear stability analysis of a generation-recombination (GR) model with two impurity levels and an estimate of the wavelengths and velocities of the expected traveling charge density waves in the regime of impurity breakdown was given in Ref. 28. More recently, a variety of simple models have been studied, including a single-level GR-model with a monotonic $j(\mathcal{E})$ characteristic[29,30] and one with an NNDC characteristic[31,32] explaining experimental findings of solitary waves in *p*-type Ge.[33] All these models have in common that they use simple phenomenological expressions for the GR rates, and that they are, in principle, of a single-level type, i.e., in addition to ''natural'' time scales such as the dielectric relaxation time or the energy relaxation time essentially only a single additional dynamic variable is entered into the equations, which drives the system's nonlinearities. Thus they cannot reproduce the SNDC characteristics observed, e.g., in *n*-type GaAs.[9] Their behavior in the nonlinear regime has been investigated either by direct simulation or by means of reduced amplitude equations, e.g., a complex Ginzburg-Landau equation.[30]

On the other hand no models have been investigated so far that are realistic enough to allow for quantitative predictions of experimental results in *p*-type Ge or especially *n*-type GaAs. A necessary condition for this is not only the use of multiple impurity levels (and thus allowing for multiple additional time scales to drive the nonlinearities, and for SNDC), but also the incorporation of expressions for the transport parameters in terms of relevant control quantities that have a solid microscopic footing. This paper's aim is to present a model that meets both of these conditions: two impurity levels together with the relevant GR kinetics between them and the conduction band are used and the GR rates are derived from a spatially homogeneous Monte Carlo (MC) simulation. With that model we offer an explanation of the small-amplitude precurser oscillations of the voltage which were recently observed at the onset of breakdown in *n*-type GaAs.[34]

The paper is organized as follows: First, we introduce our model (Sec. II). Then we perform a linear stability analysis of the model equations, and apply these results to the specific example of *n*-type GaAs (Sec. III). For *n*-type GaAs we subsequently investigate the features in the nonlinear regime by means of numerical simulation (Sec. IV) before we summarize our results (Sec. V).

II. THEORETICAL MODEL

We describe a semiconductor in the regime of low-temperature impurity breakdown by GR kinetics involving the conduction band and two donor levels.[19] In the following we refer to an *n*-type semiconductor, but the model can easily be adopted to *p*-type material by appropriate replacements. The GR processes considered are impact ionization from the donor ground state (X_1) and the excited state (X_1^*), capture into the excited level (T_1^s), ionization of the excited level (X_1^s), and relaxation (T^*) and excitation processes (X^*) between the ground state and the excited state. The GR kinetics of these processes are then described by rate equations (continuity equations in drift-diffusion approximation) for the electron concentrations in the conduction band n, in the impurity ground state n_1, and in the excited state

TABLE I. Material parameters for n-type GaAs.

Parameter	Symbol	Value
Donor concentration	N_D	7.0×10^{15} cm^{-3}
Acceptor concentration	N_A	2.0×10^{15} cm^{-3}
Lattice temperature	T_L	4.2 K
Low-field mobility	μ^*	1.54×10^{4} cm^2/V s
Relative dielectric constant	ϵ_r	10.9
Dielectric relaxation time	τ_M	7.8×10^{-14} s
Debye length	L_D	6.6×10^{-7} cm
Ionization coefficient	X_1^s	9.1639×10^{-8} (in $1/\tau_M$)
Excitation coefficient	X^*	2.6317×10^{-10} (in $1/\tau_M$)
Capture coefficient	T^*	3.2113×10^{-6} (in $1/\tau_M$)

n_2 as given in Ref. 26. Throughout this paper all variables are rendered dimensionless by normalizing all concentrations by the effective doping density $N_D^*=N_D-N_A$, where N_D is the donor density and N_A is the compensating acceptor density, and time and space by the effective dielectric relaxation time $\tau_M\equiv\epsilon_r\epsilon_0/(eN_D^*\mu^*)$ and the effective Debye length $L_D\equiv(D^*\tau_M)^{1/2}$, respectively. Electric field $\mathcal{E}$ and electron temperature are normalized by $\mathcal{E}^*\equiv k_BT_L/(eL_D)$ and by the lattice temperature T_L, respectively, where μ^* and D^* are the low-field mobility and diffusion constant, respectively.

The macroscopic transport equations are coupled to Maxwell's equations

$$\nabla\cdot\boldsymbol{\mathcal{E}}=1-n-n_1-n_2, \tag{1}$$

$$\nabla\times\boldsymbol{\mathcal{E}}=-\frac{\partial\boldsymbol{\mathcal{B}}}{\partial t}, \tag{2}$$

$$\frac{\hat{c}^2}{\epsilon_r}\nabla\times\boldsymbol{\mathcal{B}}=\boldsymbol{J}, \tag{3}$$

with $\boldsymbol{J}=\alpha\partial\boldsymbol{\mathcal{E}}/\partial t+\boldsymbol{j}$, where $\boldsymbol{J}$ is the total current-density composed of displacement current and conduction current density $\boldsymbol{j}=\mu(\mathcal{E})(n\boldsymbol{\mathcal{E}}+\nabla n)$, $\hat{c}$ is the normalized velocity of light, and ϵ_r is the relative dielectric constant. Here the parasitic wire and contact capacitances of the sample have been accounted for by adding a parallel external capacitance $C_{\rm ext}$ to the intrinsic capacitance $C_{\rm int}=\epsilon_r\epsilon_0A/L$ which introduces an additional time scale of dielectric relaxation $\alpha=1+C_{\rm ext}/C_{\rm int}$.[35] A and L are the sample cross section and length, respectively.

The essential nonlinearities of the model equations are contained in the dependence of the GR coefficients on n and $\mathcal{E}$. In order to derive these from a microscopic theory single-particle Monte Carlo (MC) simulations have been performed.[36,37] The simulated MC data are approximated by fitted analytic GR expressions as given in Refs. 26,38 and, additionally, a mobility $\mu(T_e)=0.836+2.095/[1+\exp(3.353-0.260T_e)]$ parametrized by the electron temperature $T_e(n,\mathcal{E})$. Solving the rate equations under steady state conditions for the material parameters given in Table I, we obtain $n_1(n,\mathcal{E})$ and $n_2(n,\mathcal{E})$ as functions of the electron concentration and the electric field. The S-shaped carrier-density-field characteristic (Fig. 1) for spatially homogeneous states can be obtained by substituting these expressions into the condition of local charge neutrality $n+n_1(n,\mathcal{E})+n_2(n,\mathcal{E})=1$ and solving for $n(\mathcal{E})$. The current density $j(\mathcal{E})=\mu(\mathcal{E})n(\mathcal{E})\mathcal{E}$ is shown in the inset of Fig. 1.

III. ANALYSIS OF THE LINEAR STABILITY

The behavior of the dynamic system in response to small perturbations is analyzed by a linear stability analysis where we restrict ourselves to modes which propagate in the direction of the electric field. This analysis is aimed at samples whose transverse dimensions are much smaller than their longitudinal dimension. We follow the general scheme given in Ref. 19, neglecting fluctuations of the magnetic field.

Small spatial and temporal fluctuations of the electric field and the electron concentrations around the homogeneous steady state $\{\boldsymbol{\mathcal{E}}^0,\ n^0,\ n_1^0,\ n_2^0\}$ are described by

$$\delta\boldsymbol{\mathcal{E}}(\boldsymbol{x},t)=\boldsymbol{\mathcal{E}}(\boldsymbol{x},t)-\boldsymbol{\mathcal{E}}^0, \tag{4}$$

$$\delta n(\boldsymbol{x},t)=n(\boldsymbol{x},t)-n^0, \tag{5}$$

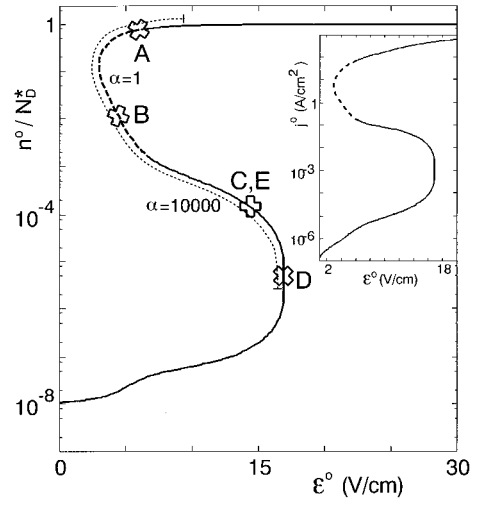

FIG. 1. Stationary carrier density n^0 as a function of electric field, calculated for n-type GaAs with the parameters given in Table I. The dashed (dotted) line shows the region which is unstable for $\alpha=1$ ($\alpha=10\,000$). The letters A, B, C, D, E denote the operating points for which time-dependent numerical solutions are shown in Figs. 5 and 6. (The inset shows the current density j versus the electric field $\mathcal{E}$.)

$$\delta n_i(\boldsymbol{x},t)=n_i(\boldsymbol{x},t)-n_i^0, \quad i=1,2. \tag{6}$$

Using the ansatz

$$\delta\boldsymbol{\mathcal{E}},\delta n,\delta n_1,\delta n_2\sim\exp(\Lambda t) \tag{7}$$

with complex eigenvalue Λ, we linearize the constitutive model equations. From equation (3) we obtain

$$\boldsymbol{\nabla}\cdot\boldsymbol{J}=\alpha\frac{\partial}{\partial t}(\nabla\cdot\boldsymbol{\mathcal{E}})+\boldsymbol{\nabla}\cdot\boldsymbol{j}=0. \tag{8}$$

The linearization of this equation with $\mu(\mathcal{E})=\mu^0+\delta\mu(\mathcal{E})$ and $\mu^0\equiv\mu(\mathcal{E}^0)$ leads to

$$\begin{aligned}0=&\alpha\Lambda\boldsymbol{\nabla}\cdot\delta\boldsymbol{\mathcal{E}}+\boldsymbol{\nabla}\cdot[n^0\mu^0\delta\boldsymbol{\mathcal{E}}+n^0\boldsymbol{\mathcal{E}}^0\delta\mu+\mu^0\boldsymbol{\mathcal{E}}^0\delta n]\\&+\boldsymbol{\nabla}\cdot[(\boldsymbol{\nabla}n^0)\delta\mu+\mu^0\boldsymbol{\nabla}\delta n]\\=&\boldsymbol{\nabla}\cdot\delta\boldsymbol{J}.\end{aligned} \tag{9}$$

From this equation we obtain the fluctuations of the total current density

$$\delta\boldsymbol{J}=(\alpha\Lambda+n^0\mu^0)\delta\boldsymbol{\mathcal{E}}+n^0\boldsymbol{\mathcal{E}}^0\delta\mu+\mu^0(\boldsymbol{\mathcal{E}}^0+\boldsymbol{\nabla})\delta n. \tag{10}$$

The next step is to substitute δn and $\delta\mu$ by the fluctuations of the electric field $\delta\boldsymbol{\mathcal{E}}$. For this purpose we decompose the fluctuations of the electric field $\delta\boldsymbol{\mathcal{E}}=(\delta\mathcal{E}_\parallel,\delta\mathcal{E}_\perp)$ into components parallel and perpendicular to the applied static field $\boldsymbol{\mathcal{E}}^0\equiv(\mathcal{E},0)$. First we eliminate δn_1 and δn_2 using the rate equations

$$\Lambda\begin{pmatrix}\delta n_1\\ \delta n_2\end{pmatrix}=\underline{\underline{B}}\begin{pmatrix}\delta n_1\\ \delta n_2\end{pmatrix}+\underline{d}\,\delta n+\underline{f}\,\delta\mathcal{E}_\parallel, \tag{11}$$

where $\underline{\underline{B}}$ is a matrix, and $\underline{d}$, $\underline{f}$ are vectors containing derivatives of the GR coefficients with regard to n or $\mathcal{E}$, respectively. The explicit expressions are given in Appendix A. It follows that

$$\begin{pmatrix}\delta n_1\\ \delta n_2\end{pmatrix}=-\frac{\mathrm{adj}(\underline{\underline{B}}-\Lambda)}{G(\Lambda)}(\underline{d}\,\delta n+\underline{f}\,\delta\mathcal{E}_\parallel), \tag{12}$$

where $G(\Lambda)=\det(\underline{\underline{B}}-\Lambda)=\Lambda^2-\Lambda\,\mathrm{tr}\underline{\underline{B}}+\det\underline{\underline{B}}$. With (12) we can rewrite the linearized Gauss law (1)

$$\nabla\cdot\delta\boldsymbol{\mathcal{E}}=-(\delta n+\delta n_1+\delta n_2), \tag{13}$$

as

$$\nabla\cdot\delta\boldsymbol{\mathcal{E}}=-\frac{H(\Lambda)}{G(\Lambda)}\delta n-\frac{F(\Lambda)}{G(\Lambda)}\delta\mathcal{E}_\parallel, \tag{14}$$

where $H(\Lambda)$ and $F(\Lambda)$ are given in Appendix A. Solving (14) for δn and observing $\delta\mu(\mathcal{E})=(\partial\mu(\mathcal{E})/\partial\mathcal{E})|_{\mathcal{E}^0}\delta\mathcal{E}_\parallel$, we obtain

$$\begin{aligned}\delta\boldsymbol{J}=&\left[(\alpha\Lambda+n^0\mu^0)-\mu^0(\boldsymbol{\mathcal{E}}^0+\nabla)\otimes\frac{G(\Lambda)}{H(\Lambda)}\nabla\cdot\right]\delta\boldsymbol{\mathcal{E}}\\&+\left[n^0\frac{\partial\mu(\mathcal{E})}{\partial\mathcal{E}}\bigg|_{\mathcal{E}^0}\boldsymbol{\mathcal{E}}^0-\mu^0(\boldsymbol{\mathcal{E}}^0+\nabla)\frac{F(\Lambda)}{H(\Lambda)}\right]\delta\mathcal{E}_\parallel,\end{aligned} \tag{15}$$

where $\otimes$ denotes the tensor product.

As we look for traveling wave instabilities we introduce the Fourier transform of $\delta\boldsymbol{\mathcal{E}}$ with regard to a wave vector $\boldsymbol{k}$ for which $\boldsymbol{k}\|\boldsymbol{\mathcal{E}}^0$ must hold for the longitudinal fluctuations investigated here:

$$\delta\boldsymbol{\mathcal{E}}=\int\delta\boldsymbol{\mathcal{E}}(\boldsymbol{k})\exp(i\boldsymbol{k}\cdot\boldsymbol{x})d^3k. \tag{16}$$

Combined with Maxwell's law of induction (2) we can prove that fluctuations $\delta\boldsymbol{J}$ are zero:

$$0=\boldsymbol{\nabla}\times(\boldsymbol{\nabla}\times\delta\boldsymbol{\mathcal{E}})=-\frac{\partial}{\partial t}(\boldsymbol{\nabla}\times\delta\boldsymbol{\mathcal{B}})=-\frac{\epsilon_r}{\hat{c}^2}\Lambda\,\delta\boldsymbol{J}. \tag{17}$$

Substituting (16) and (17) into (15) observing that all perpendicular components vanish we obtain

$$\left[(\alpha\Lambda+\widetilde{n})\frac{H(\Lambda)}{G(\Lambda)}+\mu k^2-ivk-\frac{F(\Lambda)}{G(\Lambda)}(v+ik\mu)\right]_0\delta\mathcal{E}_\parallel=0, \tag{18}$$

where $v(\mathcal{E})=\mu(\mathcal{E})\mathcal{E}$, $\widetilde{n}=n(\partial v/\partial\mathcal{E})$ and the brackets are taken at the steady state. Equation (18) can be rewritten as complex polynomial in Λ of order three which determines the dispersion relation $\Lambda(k)$:

$$(\alpha\Lambda^3+\Lambda^2t_2+\Lambda t_1+t_0)+ik(-\Lambda^2v+\Lambda u_1+u_0)=0, \tag{19}$$

where the terms t_0, t_1, t_2, u_0, u_1 are given explicitly in Appendix A.

At the bifurcation points the ansatz $\Lambda=\lambda+i\omega$ simplifies as λ must vanish. From (19) we find the following system of polynomial equations which determines the bifurcation set (neutral curve):

$$-\omega_c^2t_2-\omega_ck_cu_1+t_0=0, \tag{20}$$

$$-\alpha\omega_c^3+\omega_c^2k_cv+\omega_ct_1+k_cu_0=0, \tag{21}$$

where $\omega=\omega_c$ and $k=k_c$ denote the critical frequencies and the critical wave vectors. Note that the relation $\omega_c(k_c)=-\omega_c(-k_c)$ is always satisfied. In this case traveling waves can bifurcate only if two points $\omega_c(k_{c_1})$ and $\omega_c(k_{c_2})$ do not become undamped simultaneously for the same value of the control parameter. The latter case would lead to modulated waves.[39]

Next we solve the set of equations (20), (21) numerically for the GR coefficients of n-type GaAs as given in Ref. 26. The solution reveals which parts of the $n^0(\mathcal{E}^0)$ characteristic are unstable. Since $n^0(\mathcal{E}^0)$ is S shaped, i.e., there exist three values of n^0 in the field range between the holding field and the threshold field, it is convenient to use the steady state electron concentration n^0 as control parameter rather than the electric field.

For $\alpha=1$ ($C_{\mathrm{ext}}=0$) the instability regime is shown in Fig. 1 as a dashed line. In real samples, however, α is much larger due to parasitic wire and contact capacitances. In the experimental setup of Ref. 34, e.g., a minimum parasitic capacitance of 300 pF is found without impedance converter. It is difficult to estimate the value of α since the intrinsic capacitance $C_{\mathrm{int}}=\epsilon_r\epsilon_0A/L$ is not known. A comparison of the calculated $j(\mathcal{E})$ characteristic (Fig. 1) with the measured cur-

TABLE II. Instability regimes and critical wave vector intervals for different α.

α	$n^0_{\min}$ (N_D^*)	$n^0_{\max}$ (N_D^*)	$k_{c_{\min}}$ (cm^{-1})	$k_{c_{\max}}$ (cm^{-1})
1	1.83×10^{-3}	8.09×10^{-1}	4.1×10^{4}	3.7×10^{6}
10	5.27×10^{-6}	8.98×10^{-1}	1.6×10^{4}	7.0×10^{6}
10^2	2.89×10^{-6}	9.37×10^{-1}	2.9×10^{3}	1.2×10^{7}
10^3	2.80×10^{-6}	9.40×10^{-1}	0	2.2×10^{7}
10^4	2.94×10^{-6}	9.05×10^{-1}	0	3.8×10^{7}
5×10^4	3.05×10^{-6}	8.33×10^{-1}	0	5.2×10^{7}

rent $I=jA$ versus voltage[34] can only give a crude estimate of the effective current cross section A. Using the experimental contact distance $L=0.24$ cm and $A=10^{-2}$ cm^2, e.g., yields an intrinsic capacitance of the order of 0.04 pF, and hence $\alpha\approx10^4$. With this value of α, the instability regime is considerably enlarged, as shown by the dotted line in Fig. 1. The minimum ($n^0_{\min}$) and maximum ($n^0_{\max}$) values of the instability regime and the range of unstable wave vectors ($k_{c_{\min}}$, $k_{c_{\max}}$) in dimensional units are listed in Table II for different α. The critical wave vectors k_c and the corresponding critical frequencies ω_c are plotted in Fig. 2 as a function of the control parameter n^0 for $\alpha=1$, 10, 10^2, 10^3, 10^4, 5×10^4.

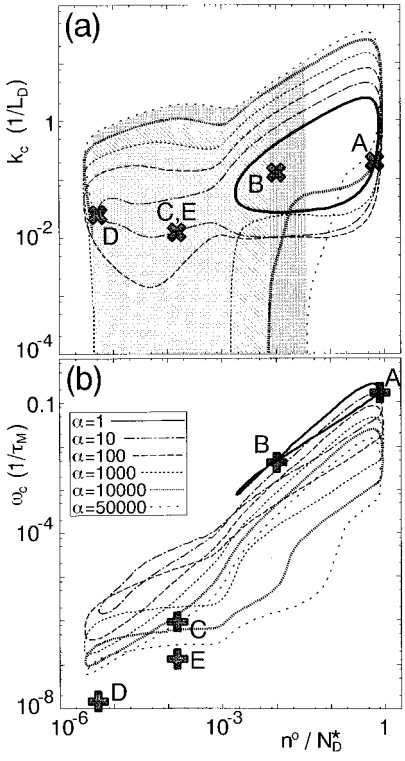

FIG. 2. (a) Critical wave vector k_c versus the control parameter n^0 (neutral curves) for different values of α (solid line: $\alpha=1$). The regions confined by the neutral curves are unstable. Hatched areas denote regimes which are unstable with respect to homogeneous relaxation oscillations. The letters A, B, C, D, E denote the points for which the nonlinear time-dependent simulations are shown in Figs. 5 and 6. (b) The critical frequencies ω_c versus the control parameter n^0. The letters A, B, C, D, E mark the frequencies estimated from the nonlinear simulation (cf. Sec. IV) for the respective points.

For $\alpha=1$, 10, 10^2 we find a closed neutral curve of k_c values, where from the dispersion relation (19) it is checked that of the three possible branches $\Lambda(k)$ only one branch is associated with unstable eigenvalues in a certain k interval. To visualize this, in Fig. 3 the branch associated with an unstable eigenvalue is plotted for $n^0\approx1.05\times10^{-6}$ (corresponding to point ''B'' in Fig. 1) and $\alpha=1$. It is undamped for finite wave vectors k in the range of $k_{c_1}<k<k_{c_2}$. Hence the closed neutral curves for $\alpha=1$, 10, 10^2 in Fig. 2 form the borders of the instability regime within which traveling waves may exist.

For larger α, e.g., $\alpha=10^3$, 10^4, 5×10^4 in Fig. 2, we find a drastic change in the bifurcation scenario. For small n^0 in the vicinity of the threshold field, we still find the traveling-wave instability with one of the three branches of $\Lambda(k)$ having a positive real part and thus being unstable between k_{c_1} and k_{c_2}. If n^0 is increased, k_{c_1} approaches zero. When k_{c_1} becomes zero, a second branch of the dispersion relation becomes undamped at $k=0$. Beyond this point, for larger n^0, two branches are undamped in the wave vector interval $0<k<k_{c_1}$ (first branch) and $0<k<k_{c_2}$ (second branch). In this regime spatially homogeneous relaxation oscillations (with $k=0$) dominate the system. These regimes are marked by different hatchings in Fig. 2. For even larger n^0 again a transition from the homogeneous relaxation oscillation regime to the traveling-waves regime occurs. The existence of these homogeneous relaxation oscillations can be physically understood as follows. These modes only occur in the NDC

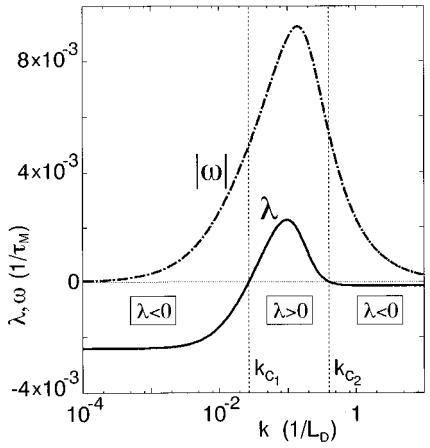

FIG. 3. Dispersion relation of the undamped branch for point B of Fig. 1 ($n^0\approx1.05\times10^{-2}$, $\alpha=1$). The real part λ (solid line) and the imaginary part ω (dashed line) of the complex eigenvalue Λ are plotted as a function of the wave vector k.

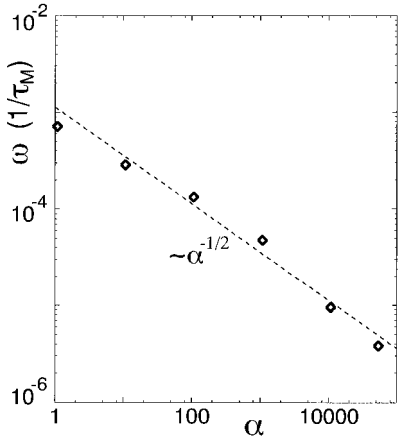

FIG. 4. Mean oscillation frequency (ω) at $n^0 \approx 2.5\times10^{-3}$ as a function of $\alpha = 1 + C_{\rm ext}/C_{\rm int}$ estimated from Fig. 2 (points). The dashed line shows the scaling law $\omega \sim \alpha^{-1/2}$.

regime of the $n^0(\mathcal{E}^0)$ characteristic, which is always unstable under voltage control. From the current conservation equation it follows $\partial\mathcal{E}_x/\partial t = \alpha^{-1}(J_x - j_x)$, where the term on the right hand side of this equation is small for large α, even if the conduction current density j_x is not close to the total current density J_x. This causes a strong delay in the response of the electric field to changes in the drift-diffusion current density and therefore to changes in the electron concentration n. Because of the instability of the NDC branch and the delayed dielectric relaxation of $\mathcal{E}_x$, the electron concentration n approaches one of the stable branches with positive differential conductivity (PDC). But with decreasing n the electric field must increase and vice versa since α is finite. If the electric field then leaves the bistability regime, e.g., by exceeding the threshold field, n increases strongly and the electric field drops below the holding field, where the electron concentration relaxes to the low-conducting branch. In this way a cycle of spatially homogeneous field and electron concentration oscillations is initiated around the stable operating point given by J_x. This mechanism of dielectric relaxation oscillations has been previously described in a variety of different models.[3,19]

From the range of wave vectors listed in Table II it is evident that the traveling-wave instabilities should be possible for sample lengths in the micrometer regime or larger. In dimensional units the frequencies lie in a range between 10^6 s^{-1} and 10^{12} s^{-1} depending on α and n^0; they increase strongly with increasing control parameter n^0. Estimating the mean frequency at $n^0 \approx 2.5\times10^{-3}$ as a function of α from Fig. 2 gives the scaling law $\omega \sim C_{\rm ext}^{-1/2}$ (Fig. 4) in agreement with general theoretical predictions.[35] Table II also reveals that for each α used here the instabilities occur both in the PDC and NDC regime.

IV. SIMULATION OF TRAVELING CARRIER-DENSITY WAVES

Since the linear stability analysis has predicted the bifurcation of traveling carrier-density waves, we shall now investigate the behavior of the spatiotemporal solutions of the full *nonlinear* system. The complete nonlinear dynamic system consists of the rate equations for n, n_1, n_2, Gauss's law (1) and the relation for the total current density $\boldsymbol{J} = \alpha\partial\boldsymbol{\mathcal{E}}/\partial t + \boldsymbol{j}$. From (3) it follows for a one-dimensional geometry that $\boldsymbol{J} \equiv (J_x,0,0)$ is spatially constant. As we consider current control, J_x can be identified as global control parameter. Since we perform 1D simulations the notation simplifies as follows: $\boldsymbol{\nabla} \rightarrow (\partial/\partial x,0,0)$, $\boldsymbol{j} \rightarrow (j_x,0,0)$, $\boldsymbol{\mathcal{E}} \rightarrow (\mathcal{E}_x,0,0)$. This simulation is not only a test of the results of the linear stability analysis, but it also shows what kind of spatiotemporal scenarios are possible when the system's nonlinearities come into play.

As solution algorithm we use an explicit Euler scheme with discrete time steps Δt and spatial discretization Δx. For times $t<0$ the system is assumed to be in a spatially homogeneous state and the controlling total current density is determined by $J_x = j_x$. At the initial time $t \equiv 0$ we choose a configuration $n(x) \equiv n^0 + \delta n(x)$ for a periodicity length L_x, where $\delta n(x) = a\sin(4\pi x/L_x)$ is a sinusoidal perturbation of the homogeneous steady state n^0 with an amplitude $a \equiv 10^{-3}\times n^0$ that meets periodic boundary conditions, i.e., $\delta n(x+L_x) = \delta n(x)$. Thus the periodicity length L_x contains two periods of the perturbation, and a local charge neutrality in most points no longer holds, while global charge neutrality is conserved. Such periodic boundary conditions mimic infinitely extended samples if the largest wavelengths of the spatial structures are smaller than the periodicity length L_x. Since the initial conditions must meet Poisson's equation, the electric field $\mathcal{E}_x(t=0)$ is also a sinusoidal perturbation but with a phase shift of $(-\pi/2)$. This procedure is justified by the assumption that the electric field follows the perturbation instantaneously. To propagate the system forward in time, we determine the values n^{i+1}, n_1^{i+1}, and n_2^{i+1} from the values of the ith iteration by the rate equations. In the same way $\mathcal{E}_x^{\,i+1}$ is determined from $J_x = \alpha\partial\mathcal{E}_x/\partial t + j_x$. From these $(i+1)$th values the current density j_x^{i+1} is finally calculated. A time increment Δt and a spatial discretization Δx is used.

We present simulation results for five operating points on the $n^0(\mathcal{E}^0)$ characteristic denoted by ''A,'' ''B,'' ''C,'' ''D,'' and ''E'' (cf. Fig. 1) . Point A represents a state with positive differential conductivity at the onset of the high-conducting branch ($n^0 \approx 0.75$, $\mathcal{E}^0 = 6\,V/\mathrm{cm}$) without an external capacity, i.e., $\alpha = 1$. We choose a periodicity length of $L_x = 50$ which corresponds to a wave vector $k = 4\pi/L_x \approx 0.25$ of the initial perturbation lying in the instability regime of Fig. 2(a). For this case the simulation results for the electron density and the electric field are shown in Fig. 5(a) and Fig. 6(a), respectively. We obtain traveling waves propagating at constant phase velocity. However, at about $t = 200$, the initial spatial and temporal period is suddenly cut by half. This superharmonic frequency doubling bifurcation appears to occur when the nonlinearities come into play. At the same time the donor levels are no longer populated homogeneously in space, since the initial perturbation of n induces spatial modulations of n_1 and n_2 due to their coupling by the GR processes. Nevertheless the initial phase shift of $(-\pi/2)$ between the perturbations of n and $\mathcal{E}_x$ is conserved. The frequency of the superharmonic nonlinear waves is estimated as $\omega \approx 0.2$ which is consistent with the linear stability analysis in Fig. 2(b).

Point B corresponds to a negative differential conductiv-

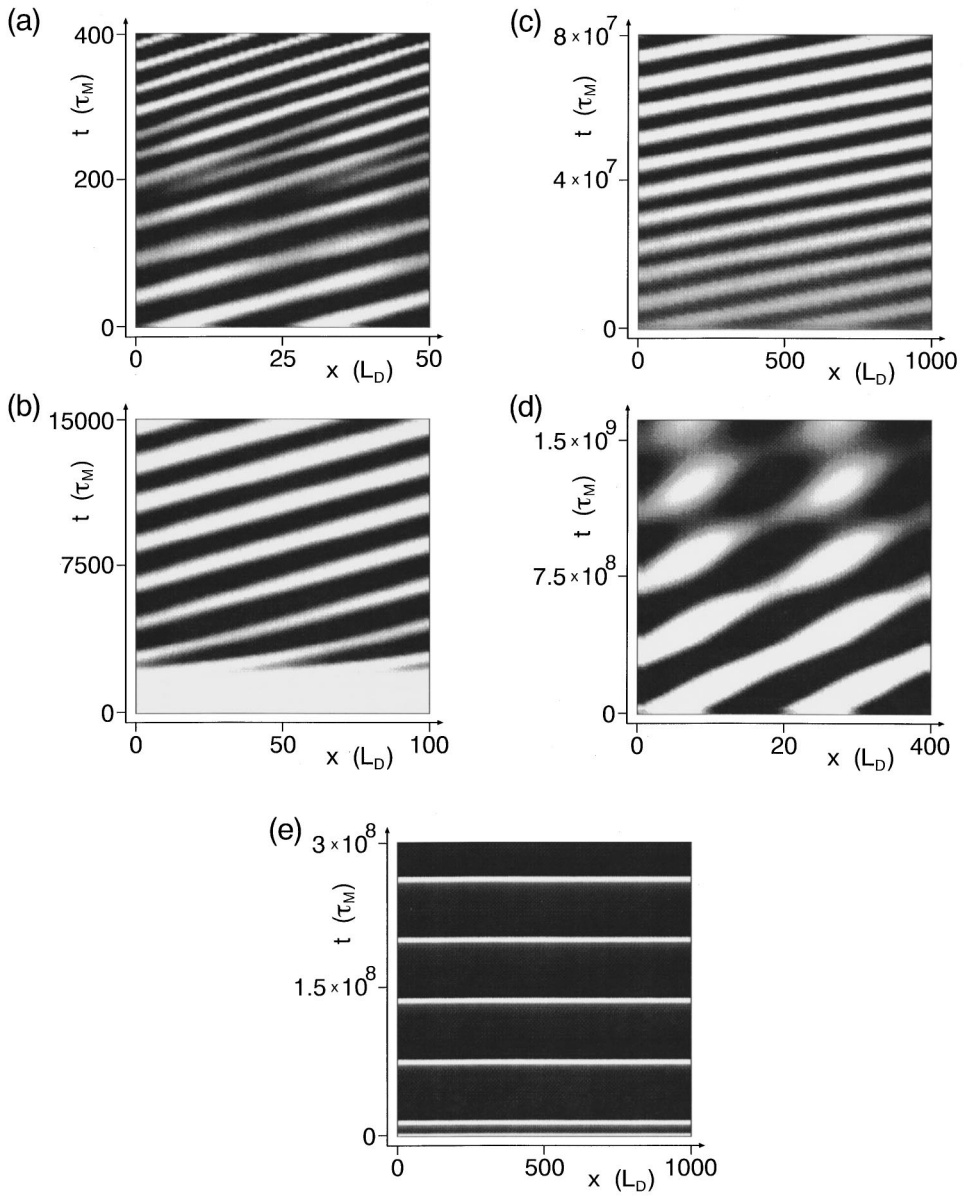

FIG. 5. Spatiotemporal dynamics of the carrier density n for points A, B, C, D, E of Fig. 1. Darker areas indicate lower densities whereas brighter areas indicate higher densities. (a) Point A ($\mathcal{E}^0=6$ V/cm, $n^0=7.520\times10^{-1}$, $n_1^0=1.537\times10^{-2}$, $n_2^0=2.326\times10^{-1}$, $L_x=50$, $\Delta x=0.5$, $\Delta t=0.02$, $\alpha=1$). (b) Point B ($\mathcal{E}^0=4.5$ V/cm, $n^0=1.048\times10^{-2}$, $n_1^0=9.182\times10^{-1}$, $n_2^0=7.131\times10^{-2}$, $L_x=100$, $\Delta x=1$, $\Delta t=1$, $\alpha=1$). (c) Point C ($\mathcal{E}^0=14$ V/cm, $n^0=1.667\times10^{-4}$, $n_1^0=9.957\times10^{-1}$, $n_2^0=4.148\times10^{-3}$, $L_x=1000$, $\Delta x=10$, $\Delta t=100$, $\alpha=100$). (d) Point D ($\mathcal{E}^0=17.029$ V/cm, $n^0=4.991\times10^{-6}$, $n_1^0=9.997\times10^{-1}$, $n_2^0=2.452\times10^{-4}$, $L_x=400$, $\Delta x=8$, $\Delta t=80$, $\alpha=100$). (e) Point E ($\mathcal{E}^0=14$ V/cm, $n^0=1.667\times10^{-4}$, $n_1^0=9.957\times10^{-1}$, $n_2^0=4.148\times10^{-3}$, $L_x=1000$, $\Delta x=10$, $\Delta t=100$, $\alpha=10\,000$).

ity state with $n^0\approx1.05\times10^{-2}$ and $\mathcal{E}^0=4.5$ V/cm and with $\alpha=1$. The periodicity length L_x is chosen as $L_x=100$ to match the unstable initial wave vector $k\approx0.12$ [see Fig. 2(a)]. The simulation results shown in Figs. 5(b) and 6(b) reveal a strong increase of the initial perturbation amplitude after $t\approx2000$, which is due to a decrease of the electric field below the holding field, where the negative differential conductivity branch no longer exists and the only stable state is the low-conducting state. Therefore the trapping of electrons is strongly enhanced. The conservation of the total current then again enforces an increase of the electric field leading to strong spatiotemporal oscillations of n and $\mathcal{E}_x$. During this process the initial periodicity in space and time is conserved, as is the phase shift between electric field $\mathcal{E}_x$ and electron density n. From the simulation results we estimate the frequency of the traveling waves as $\omega\approx3.8\times10^{-3}$, which is very close to the prediction of the frequencies from the linear stability analysis in Fig. 2(b).

For point C an external capacity is considered by using $\alpha=100$. The steady state electron concentration is $n^0\approx1.67\times10^{-4}$ and the corresponding field is $\mathcal{E}^0=14$ V/cm. The linear stability analysis [cf. Fig. 2(a)] for $\alpha=100$ also predicts the existence of traveling waves at this operating point (whereas for $\alpha=1$ it is stable). This is confirmed by simulations for these parameters with a periodicity length of $L_x=100$ corresponding to a wave vector of $k\approx0.012$ [Figs. 5(c) and 6(c)]. The amplitude of the initial perturbation of n which is 1/1000 of the steady state electron concentration

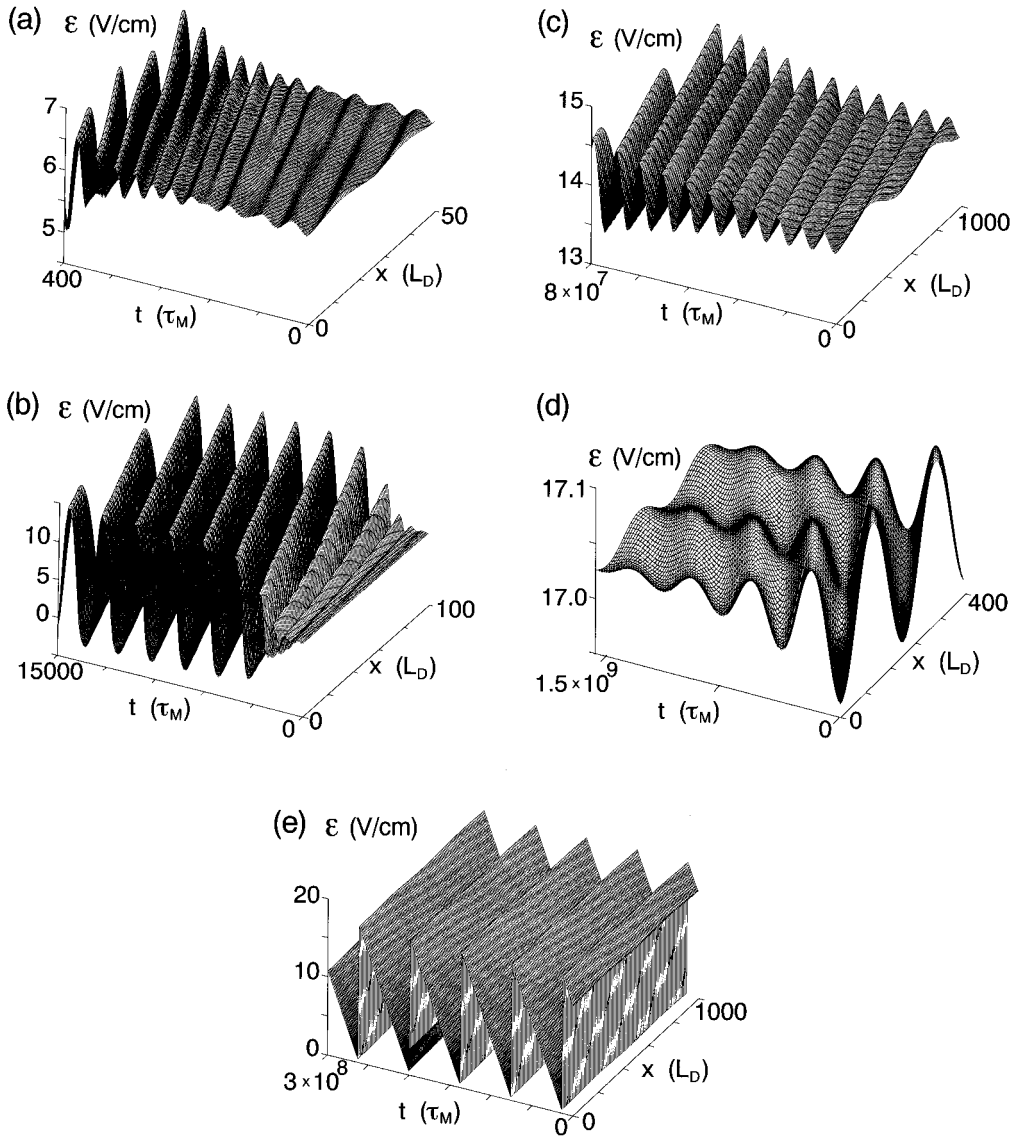

FIG. 6. Spatiotemporal dynamics of the electric field $\mathcal{E}_x$. Parameters as in Fig. 5(a)–(e).

n^0 rapidly grows while the perturbation starts traveling through the sample. We find an oscillatory behavior with fixed period and a slightly increasing amplitude. After $t=8\times10^7$ the amplitude is 6/100 of n^0 and has thus grown by a factor of 60. The electric field distribution shows the same structure but with a phase shift of $\pi/2$. Estimating the frequency $\omega\approx8\times10^{-7}$ ($f\approx1.6$ MHz in dimensional units) of the traveling waves from the simulation leads to a slightly lower value than expected from the linear stability analysis [Fig. 2(b)].

Point *D* lies close to the threshold field beyond which impurity breakdown occurs. The electron concentration is as low as $n^0\approx5\times10^{-6}$ and the corresponding field is $\mathcal{E}^0=17.029$ V/cm. The control parameter α is chosen as $\alpha=100$. Here we also find traveling waves with an even lower frequency $\omega\approx2\times10^{-8}$ ($f\approx40$ kHz in dimensional units) [Figs. 5(d) and 6(d)]. These waves show additional modulations due to the coupling with the spatially inhomogeneous occupation of the donor ground state as a result of the spatially inhomogeneous initial perturbation. The reason is the very low electron density which makes the electrons rather susceptible to changes in n_1 which occur on a much longer time scale.

Point *E* corresponds to the same parameters as for point *C*, except for the external capacitance. Here α is set equal to $\alpha=10\,000$ where we expect the dominance of the $k=0$ modes leading to spatially homogeneous relaxation oscillations. These are indeed found in the simulations [Figs. 5(e) and 6(e)]. Between the narrow white stripes and the broad dark areas in Fig. 5(e) the electron concentration changes by a factor of $\approx10^5$ leading to sharp spikes in which the sample becomes highly conducting. This, together with the slow sawtoothlike rise of the electric field is typical of relaxation oscillations. The frequencies $\omega\approx10^{-7}$ ($f\approx200$ kHz in dimensional units) are one order of magnitude smaller than for point *C*, as expected from the scaling law for α (Fig. 4).

V. DISCUSSION

We have shown for a semiconductor model describing low-temperature impurity breakdown with an *S*-shaped

current-density-field characteristic that traveling-wave instabilities may arise not only on branches with negative differential conductivity, but also at the onset of the high conductivity branch with positive differential conductivity. These predictions from a linear stability analysis have been confirmed by simulations of the full *nonlinear* system of the underlying model equations. The simulations have revealed a variety of spatiotemporal instabilities ranging from the generation of sinusoidal harmonic and frequency-doubled traveling waves to spatially uniform large-amplitude relaxation oscillations. Furthermore, we have shown that the value of the contact and parasitic capacity plays a crucial role in the bifurcation behavior and the system's stability. We have seen that this spatiotemporal behavior strongly depends on the nonlinear coupling of the underlying GR processes with the donor levels. Thus the different spatiotemporal behavior and the occurrence of large amplitudes for states close to the holding or threshold field can be understood in terms of the interaction of these states with the low-conducting and high-conducting branch of the *S*-shaped characteristic.

Moreover, our simulations offer an explanation of the sinusoidal periodic oscillations with a small amplitude (''precursor oscillations'') which were recently observed experimentally in *n*-type GaAs just below the onset of breakdown.[34] Their amplitude grows with increasing current as expected for a supercritical Hopf bifurcation. The frequency was found to scale with the external capacitance C as $C^{-1/2}$, e.g., 140 kHz were observed at $C=300$ pF. All these features are in good agreement with the traveling waves found, e.g., at point C and D [Figs. 5(c,d) and 6(c,d)]. As shown by our stability analysis, they are indeed generated by a Hopf bifurcation at finite wave vector k. Upon further increase of the current, large-amplitude nonlinear relaxation oscillations were observed in experiment.[34] Indeed our simulations yield these homogeneous relaxation oscillations for sufficiently large α [e.g., point E: Figs. 5(e) and 6(e)]. As is evident from Fig. 2(a), for such large values of α, this $k=0$ relaxation oscillation mode dominates in a broad regime of n^0 values (hatched areas), while traveling-wave ''precursor'' oscillations can exist only in a very narrow interval of n^0, i.e., currents, preceding this relaxation regime at the onset of breakdown, as observed experimentally.

ACKNOWLEDGMENTS

We thank T. Christen and V. Novák for enlightening discussions and, in particular, R. E. Kunz for his collaboration during the initial stages of this work.

APPENDIX: AUXILIARY FORMULAS

Here we list explicit expressions which are used in Sec. III. In the following ∂_n and $\partial_{\mathcal{E}}$ denote the partial derivatives with respect to n and $\mathcal{E}$, respectively.

$$\underline{\underline{B}}=\begin{pmatrix} -X^*-X_1 n & T^* \\ X^*-T_1^s n & -T^*-X_1^s-T_1^s n-X_1^* n \end{pmatrix}, \tag{A1}$$

$$\underline{d}=\begin{pmatrix} -[X_1+(\partial_n X_1)n]n_1 \\ [T_1^s+(\partial_n T_1^s)n](1+c-n_1-n_2)-[X_1^*+(\partial_n X_1^*)n]n_2 \end{pmatrix}, \tag{A2}$$

$$\underline{f}=\begin{pmatrix} -(\partial_{\mathcal{E}} X_1)n_1 n \\ (\partial_{\mathcal{E}} T_1^s)(1+c-n_1-n_2)n-(\partial_{\mathcal{E}} X_1^*)n_2 n \end{pmatrix}, \tag{A3}$$

$$\begin{aligned} H(\Lambda)&=G(\Lambda)-\sum_{i,j=1}^{2}(\mathrm{adj}(\underline{\underline{B}}-\Lambda))_{ij}d_j \\ &=\det(\underline{\underline{\tilde{A}}}-\Lambda)=\Lambda^2-\Lambda\,\mathrm{tr}\underline{\underline{\tilde{A}}}+\det\underline{\underline{\tilde{A}}}, \end{aligned} \tag{A4}$$

with

$$\tilde{A}_{ij}=B_{ij}-d_i, \tag{A5}$$

and

$$\begin{aligned} F(\Lambda)&=-\sum_{i,j=1}^{2}(\mathrm{adj}(\underline{\underline{B}}-\Lambda))_{ij}f_j \\ &=[(\Lambda+B_{21}-B_{22})f_1+(\Lambda+B_{12}-B_{11})f_2] \qquad \text{(A6)} \\ &\equiv-\Lambda\alpha_1-\alpha_2, \qquad \text{(A7)} \end{aligned}$$

where

$$\alpha_1=-(f_1+f_2), \tag{A8}$$

$$\begin{aligned} \alpha_2=-\{&[T^*+X_1^s+X^*+X_1^*(n,\mathcal{E})n]f_1 \\ &+[T^*+X^*+X_1(n,\mathcal{E})n]f_2\}. \end{aligned} \tag{A9}$$

$$t_2=\tilde{n}-\alpha\,\mathrm{tr}\underline{\underline{\tilde{A}}}+\mu k^2, \tag{A10}$$

$$t_1=\alpha\det\underline{\underline{\tilde{A}}}-\tilde{n}\,\mathrm{tr}\underline{\underline{\tilde{A}}}+v\alpha_1-\mu k^2\mathrm{tr}\underline{\underline{B}}, \tag{A11}$$

$$t_0=\tilde{n}\det\underline{\underline{\tilde{A}}}+v\alpha_2+\mu k^2\det\underline{\underline{B}}, \tag{A12}$$

and

$$u_1=\mu\alpha_1+v\,\mathrm{tr}\underline{\underline{B}}, \tag{A13}$$

$$u_0=\mu\alpha_2-v\det\underline{\underline{B}}. \tag{A14}$$

[1] M. C. Cross and P. C. Hohenberg, Rev. Mod. Phys. **65**, 851 (1993).

[2] A. S. Mikhailov, *Foundations of Synergetics 1*, 2nd ed. (Springer, Berlin, 1994).

[3] E. Schöll, in *Handbook on Semiconductors*, 2nd ed., edited by P. T. Landsberg (North-Holland, Amsterdam, 1992), Vol. 1.

[4] *Nonlinear Dynamics in Solids*, edited by H. Thomas (Springer, Berlin, 1992).

[5] *Nonlinear Dynamics and Pattern Formation in Semiconductors and Devices*, edited by F. J. Niedernostheide (Springer, Berlin, 1995).

[6] K. Aoki and T. Kondo, Phys. Lett. A **145**, 281 (1991).

[7] A. Brandl and W. Prettl, Phys. Rev. Lett. **66**, 3044 (1991).

[8] J. Peinke, J. Parisi, O. Rössler, and R. Stoop, *Encounter with Chaos* (Springer, Berlin, 1992).

[9] J. Spangler, U. Margull, and W. Prettl, Phys. Rev. B **45**, 12 137 (1992).

[10] J. Spangler, B. Finger, C. Wimmer, W. Eberle, and W. Prettl,

Semicond. Sci. Technol. **9**, 373 (1994).
[11] B. K. Ridley, Proc. Phys. Soc. **82**, 954 (1963).
[12] M. Büttiker and H. Thomas, Z. Phys. B **34**, 301 (1979).
[13] L. L. Bonilla, Phys. Rev. B **45**, 11 642 (1992).
[14] R. Döttling and E. Schöll, Physica D **67**, 418 (1993).
[15] R. Döttling and E. Schöll, Solid-State Electron. **37**, 685 (1994).
[16] F. Prengel, A. Wacker, and E. Schöll, Phys. Rev. B **50**, 1705 (1994).
[17] L. L. Bonilla, J. Galan, J. A. Cuesta, F. C. Martinez, and J. M. Molera, Phys. Rev. B **50**, 8644 (1994).
[18] A. Wacker, G. Schwarz, F. Prengel, E. Schöll, J. Kastrup, and H. T. Grahn, Phys. Rev. B **52**, 13 788 (1995).
[19] E. Schöll, *Nonequilibrium Phase Transitions in Semiconductors* (Springer, Berlin, 1987).
[20] F.-J. Niedernostheide, M. Arps, R. Dohmen, H. Willebrand, and H.-G. Purwins, Phys. Status Solidi B **172**, 249 (1992).
[21] G. Hüpper, K. Pyragas, and E. Schöll, Phys. Rev. B **48**, 17 633 (1993).
[22] G. Hüpper, K. Pyragas, and E. Schöll, Phys. Rev. B **47**, 15 515 (1993).
[23] A. Wacker and E. Schöll, Z. Phys. B **93**, 431 (1994).
[24] B. S. Kerner and V. V. Osipov, *Autosolitons* (Kluwer, Dordrecht, 1994).
[25] V. Novák, C. Wimmer, and W. Prettl, Phys. Rev. B **52**, 9023 (1995).
[26] M. Gaa, R. E. Kunz, and E. Schöll, Phys. Rev. B **53**, 15 971 (1996).
[27] E. Schöll, Phys. Scr. **T29**, 152 (1989).
[28] P. Andrich, Master's thesis, RWTH Aachen, 1988.
[29] T. Christen, Phys. Rev. B **49**, 16 423 (1994).
[30] T. Christen, Z. Phys. B **97**, 473 (1995).
[31] I. R. Cantalapiedra, L. L. Bonilla, M. J. Bergmann, and S. W. Teitsworth, Phys. Rev. B **48**, 12 278 (1993).
[32] M. J. Bergmann, S. W. Teitsworth, L. L. Bonilla, and I. R. Cantalapiedra, Phys. Rev. B **53**, 1327 (1996).
[33] A. M. Kahn, D. J. Mar, and R. M. Westervelt, Phys. Rev. B **43**, 9740 (1991).
[34] U. Margull, Ph.D. thesis, Universität Regensburg, 1996.
[35] A. Wacker and E. Schöll, J. Appl. Phys. **78**, 7352 (1995).
[36] B. Kehrer, W. Quade, and E. Schöll, Phys. Rev. B **51**, 7725 (1995).
[37] H. Kostial, M. Asche, R. Hey, K. Ploog, B. Kehrer, W. Quade, and E. Schöll, Semicond. Sci. Technol. **10**, 775 (1995).
[38] M. Gaa, R. E. Kunz, and E. Schöll, in *Proceedings of the 9th International Conference on Hot Carriers in Semiconductors*, edited by K. Hess, J. P. Leburton, and U. Ravaioli (Plenum, New York, 1996), pp. 347–351.
[39] S. Thiesen and H. Thomas, Z. Phys. B **65**, 397 (1987).